CrossMark

Onset of Plasmoid Reconnection during Magnetorotational Instability

Jarrett Rosenberg[1,2] and Fatima Ebrahimi[1,3]
[1] Princeton Plasma Physics Laboratory, Princeton University, Princeton, NJ, 08543, USA
[2] Department of Physics, Applied Physics, and Astronomy, Rensselaer Polytechnic Institute, Troy NY, 12180, USA
[3] Department of Astrophysical Sciences, Princeton University, Princeton, NJ, 08544, USA

Abstract

The evolution of current sheets in accretion flows undergoing magnetorotational instability (MRI) is examined through two- and three-dimensional numerical modeling of the resistive MHD equations in global cylindrical geometry. With an initial uniform magnetic field aligned in the vertical (z) direction, MRI produces radially extended toroidal (azimuthal) current sheets. In both 2D and 3D when axisymmetric modes dominate, these current sheets attract each other and merge in the poloidal (rz) plane, driving magnetic reconnection when the Lundquist number $S > 3 \times 10^2$, making it a possible source of plasmoids (closed magnetic loops) in accretion disks. At high Lundquist numbers in the 2D regime, starting at $S = 5 \times 10^3$, self-consistent MRI-generated current sheets become thin and subject to plasmoid instability, and therefore spontaneous magnetic reconnection. When nonaxisymmetric 3D modes dominate, turbulence makes the azimuthal current sheets more unstable and stretch vertically. Toroidally extended vertical current sheets in the inner region, as well as larger 3D magnetic islands in the outer regions of the disks are also formed. These findings have strong ramifications for astrophysical disks as potential sources of plasmoids that could cause local heating, particle acceleration, and high energy EM radiation.

Unified Astronomy Thesaurus concepts: Magnetohydrodynamical simulations (1966); Magnetic fields (994); Plasma astrophysics (1261)

1. Introduction

Accretion disks power many of the most luminous astrophysical objects, including X-ray binaries, accreting black hole sources, quasars, and gamma-ray bursts. As matter accretes from astrophysical disks onto a central body, angular momentum is rapidly transported outward. In these differentially rotating systems, weak magnetic fields can trigger turbulence via the magnetorotational instability (MRI), transporting angular momentum outward by harnessing Maxwell stress (Balbus & Hawley 1991). In addition to the dynamics of angular momentum transport, magnetic fields also drive other high energy processes in astrophysical disks, including the poloidal collimation of jets resulting from fields in the disk. Continued observational discoveries of high energy emission and jets from accretion flows around black hole engines, in particular recent observational evidence of weak, large-scale magnetic fields in disks (Event Horizon Telescope Collaboration et al. 2021), highlight the fundamental role of magnetic fields in explaining many of the most luminous sources in the universe. In this Letter, we examine whether magnetic fields and the resulting currents from a flow-driven instability such as MRI could directly provide sites for fast magnetic reconnection in accretion flows.

Magnetic reconnection, the rearrangement of magnetic field topology, is a ubiquitous process in nature, which energizes magnetically dominated plasmas such as solar flares, and is being extensively studied through observations (Fox et al. 2016) and experiments (Zweibel & Yamada 2009; Ji et al. 2020, and references therein), as well as for space application (Ebrahimi 2020). Reconnection also plays a critical role in disk corona regions (Uzdensky 2011 and references therein) and the creation of flux ropes. In the context of MRI turbulence in shearing box geometry, channel flows (Hawley & Balbus 1992) have been found to be subject to parasitic instabilities such as magnetic tearing-mode reconnection (Goodman & Xu 1994; Latter et al. 2009). Reconnection and secondary tearing instabilities have also been investigated using axisymmetric MRI simulations (Tatsuno & Dorland 2008) and in the context of MRI experiments (Liu et al. 2006). However, studies of magnetic reconnection in flow-dominated accreting systems still remain limited. The role of turbulent reconnection in accretion disks has been investigated using shearing box simulations (Kadowaki et al. 2018), and has also been suggested to be responsible for the radio and gamma-ray emission from accreting black holes (Singh et al. 2015; Ripperda et al. 2020). Joule heating and X-ray luminosity have also been associated with the energy release due to magnetic reconnection in the innermost plunging region of black hole accretion disks (Machida & Matsumoto 2003). In protoplanetary disks, the location of current sheets and their distribution may also be important for intermittent heating of these disks (Hubbard et al. 2012).

In these flow-dominated systems, the question arises whether fluctuations from flow-driven instabilities could directly cause spontaneous plasmoid reconnection. Magnetic reconnection is characterized by oppositely directed field lines, separated by a current layer, pinched into an X-point (Petschek 1964) along with a magnetic island, or plasmoid, formation. When the local Lundquist number (defined as $S = LV_a/\eta$, where L is the length of the local current sheet, $V_a = B_0/\sqrt{\mu_0\rho}$ is the Alfvén speed based on the local reconnecting magnetic field strength B_0, and η is the magnetic diffusivity) becomes sufficiently large, on the order of 10^4, thin current sheets are subject to plasmoid instability, or plasmoid reconnection, in which they break up into multiple plasmoids and X-points (Biskamp 1986; Tajima & Shibata 1997; Loureiro et al. 2007).

In this Letter we examine the underlying physics of accretion flows and whether there are reconnection sites generated by the primary MRI that could trigger fast plasmoid reconnection. We employ a global resistive MHD disk model, a hollow cylinder threaded by a weak vertical magnetic field. In particular, we

(a)

(b)

(c)

(d)
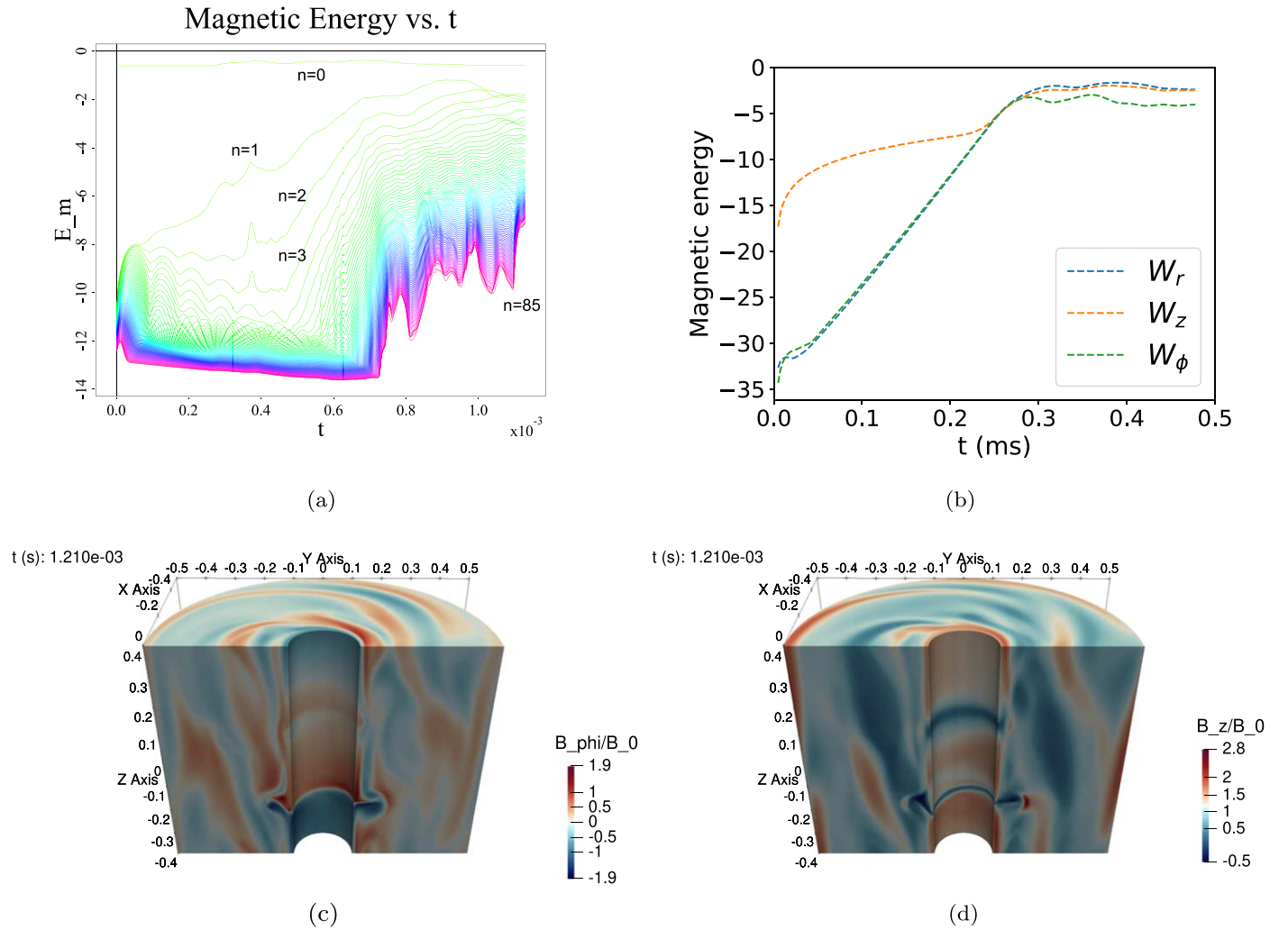
Figure 1. The log of the total magnetic energy with respect to time for each toroidal Fourier mode is given in (a) for the 3D case. The top curve is the $n = 0$ mode, the next one down is the $n = 1$, and so on. The log of volume averaged magnetic energy $W_i = 1/2\mu_0 V \int (B_i - B_{i0})^2 dV$, where B_{i0} is the value of the field component at $t = 0$, is plotted in (b) early in time for the $n = 0$ mode, broken down by component. A poloidal cut of the cylinder late in time, colored by B_ϕ, is displayed in (c). A poloidal cut of the cylinder late in time, colored by B_z, is similarly displayed in (d).

focus on the formation and evolution of current sheets under MRI, and their involvement in reconnection events, for low and high Lundquist numbers and in two and three dimensions. To identify the reconnection sites and X-points in 2D and 3D, we utilize Poincaré plots in the poloidal plane (the intersection of field lines with the rz plane as the field is followed around azimuthally), as well as in the toroidal xy planes. Through this field line tracing, we find that 2D plasmoids (and 3D magnetic islands) are formed both through driven reconnection (i.e., via merging current sheets from MRI turbulent motions), as well as through spontaneous plasmoid reconnection due to current sheet instabilities driven by MRI.

2. Simulation Setup

To simulate an accretion disk subject to MRI, we use the Non-Ideal Magnetohydrodynamics with Rotation, an Open Discussion project (NIMROD) code (Sovinec et al. 2004), which solves the three-dimensional nonlinear extended MHD equations in toroidal axisymmetric, cylindrical, or Cartesian slab geometry using a pseudo-spectral method. For our MRI simulations presented in this paper, we employ an MHD model

with explicit resistivity and with a similar simulation setup as described in Ebrahimi et al. (2011).

We model the accretion disk as an unstratified Keplarian cylinder with an impenetrable hollow center where the supermassive object would normally sit (see Figures 1(c) and 1(d) for reference on the general geometry of our disk). We do not include gravity in our model, as we are only interested in the MRI and its associated plasma physics, and instead balance the momentum equation with a pressure gradient $\nabla p = \rho V_\phi^2 / r$. We simulate a deuterium plasma with a number density of $10^{19} \, \text{m}^{-3}$ (all the quantities in NIMROD are in physical SI units). The relevant magnetic diffusivities η used in our simulations are given in Table 1. Across our simulations we cover a range of magnetic Reynolds numbers, from 10^3–10^5 (see Table 1), defined as $R_m = HV_{\phi 0}/\eta$, where $H = z_2 - z_1$ is the cylinder height and $V_{\phi 0}$ is the initial toroidal flow at the inner boundary. The local Lundquist numbers S have also been computed shortly after current sheet formation, using B_r (radial magnetic field perturbation fully generated by MRI) near the sheets for the Alfvén speed, and included in the table. The magnetic Prandtl number, defined as $P_m = \nu/\eta$ where ν is the viscosity, was kept at unity across all simulations.

Table 1
Initial Parameters and Calculated Values for Simulated Disks

ID #	# of Toroidal Modes N	Aspect Ratio H/R	η (m^2 s^{-1})	R_m $HV_{\phi 0}/\eta$	S LV_a/η	γ/Ω_0	Poloidal Resolution $r \times z$ polynomial deg.
P1	1	0.44	5	2.53×10^3	2.81×10^2	0.259	40×40 (80×80) deg. 5
P2	1	0.44	2	6.32×10^3	6.59×10^2	0.282	40×40 deg. 5
P3	1	0.44	1	1.26×10^4	1.11×10^3	0.291	40×40 (80×60) deg. 5
P4	1	0.44	0.5	2.53×10^4	2.66×10^3	0.301	40×40 (80×80) deg. 6
P5	1	0.44	0.2	6.32×10^4	5.12×10^3	0.307	80×40 deg. 6
P6	1	0.44	0.1	1.26×10^5	1.02×10^4	0.310	80×60 deg. 6
O1	1	2	5	5.06×10^3	2.90×10^2	0.255	40×40 deg. 5
O2	1	2	2	1.26×10^4	7.80×10^2	0.280	40×40 deg. 5
O3	1	2	1	2.53×10^4	1.26×10^3	0.296	40×40 (80×80) deg. 5
O4	1	2	0.5	5.06×10^4	2.36×10^3	0.297	40×40 (80×80) deg. 6
O5	1	2	0.2	1.26×10^5	5.37×10^3	0.304	80×80 (120×120) deg. 6
O6	1	2	0.1	2.53×10^5	1.12×10^4	0.310	80×80 deg. 6
O7	1	2	0.05	5.06×10^5	1.40×10^4	0.318	120×120 deg. 6
	86 (3D)	2	2	1.01×10^4	6.24×10^2	0.237	40×40 deg. 4

Note. Local S is computed shortly after current sheet formation, prior to plasmoid formation. In the 3D case, S was computed at $t = 0.32$ ms. In the resolution column, the parentheses indicate the higher resolution used to verify the results.

We use a finite element discretization in the poloidal plane (rz). We give the numerical resolution of our simulations in Table 1, which we define as the number of elements in r by z, along with the polynomial degree. We use a spectral, discrete Fourier transform in the toroidal (ϕ) direction. Variables, including the physical fields, flow velocity, and magnetic field are thus represented in standard cylindrical coordinates (r, ϕ, z) and have the following form:

$$f(r, \phi, z, t) = f_0(r, z, t) + \sum_{n=1}^{N-1}[f_n e^{\mathrm{in}\phi} + f_n^* e^{-\mathrm{in}\phi}],$$

where N is the total number of toroidal modes included, and f_n are complex functions of r, z, and t. To study reconnection physics, we performed several 2D, axisymmetric simulations with varying explicit resistivities,[4] achieved by only evolving the $n = 0$ mode ($N = 1$). To study the impact of 3D, nonaxisymmetric effects, we carried out one simulation with $N = 86$ toroidal modes. The toroidal plasma flow at the boundaries are specified to drive flow, and a no-slip condition is used for the poloidal flow. The cylinder walls are perfectly conducting. The toroidal and vertical (z) directions are periodic.

We should note that, in order to verify our results, we took a subset of our 2D simulations with varying resistivities and doubled the poloidal resolution (see Table 1), and we found no significant changes in our results. Due to time and resource constraints, we did not check our 3D simulation in the same fashion for the poloidal resolution. Thus, while the 3D results should be reliable early in time in the 2D regime, the number of reconnection sites might require further verification later in time at higher resolution. As we are interested in the global nature of reconnection sites and for the sake of completeness, we will show some of the interesting results from the 3D simulation at the end of this paper. A more thorough study of reconnection in the turbulent regime with higher resolution will be investigated in a future work.

To trigger MRI in our simulations, we seed the disk with a uniform magnetic field aligned in the z direction, and impose an

initial Keplarian toroidal flow of the form $V_\phi \propto r^{-1/2}$. The initial profiles, including the magnitude of the magnetic field, in the simulations are chosen to be unstable to MRI in the MHD regime (with $B_0 = 0.001T$), and have been benchmarked with the local WKB dispersion relation to produce a sufficiently large growth rate (see Ebrahimi et al. 2011, Figure 6). The MRI linear growth rate γ, normalized to the initial inner angular velocity Ω_0, has also been computed for each simulation and included in Table 1.

For our 2D study, we examined two types of cylinders: one with dimensions $0.1\,\mathrm{m} \leqslant r \leqslant 0.5\,\mathrm{m}$ and $-0.4\,\mathrm{m} \leqslant z \leqslant 0.4\,\mathrm{m}$, and the other with $0.1\,\mathrm{m} \leqslant r \leqslant 1\,\mathrm{m}$ and $-0.2\,\mathrm{m} \leqslant z \leqslant 0.2\,\mathrm{m}$. Defining the aspect ratio to be $H/(r_2 - r_1)$, the former has a ratio of 2.0 and the latter a ratio of 0.44. We shall refer to these two cylinders by their aspect ratio going forward. For our 3D disk, we use aspect ratio 2.0.

3. Results and Analysis

We began our study by performing the full 3D simulation of standard MRI in global cylindrical geometry as described above. Figure 1(a) shows the evolution of total magnetic energy in the 3D simulation, separated by mode, with respect to time. Figure 1(b) is the energy of each component of the axisymmetric $n = 0$ mode early in time, where the mean initial B_{z0} has been subtracted from $B_z(t)$. The axisymmetric MRI $n = 0$ mode grows exponentially (with $\gamma/\Omega_0 = 0.237$) and saturates relatively quickly, at time $t = 0.3$ ms. Many of the higher, nonaxisymmetric modes are nonlinearly triggered and saturate around $t = 0.7$ ms. As is seen from the modal energy and spectrum in Figure 1(a), this 3D simulation is well resolved in the toroidal direction.

For reference, an image of the top and inner plane of the cylinder is shown in Figures 1(c) and (d), late in time, at which point the system has become turbulent from higher modes saturating. Note that the magnitude of B_ϕ has become twice as strong as the starting vertical field in some spots, and the magnitude of B_z has increased to almost triple its starting value. This is a clear indication of dynamo action as a result of MRI induced turbulence (Brandenburg et al. 1995; Rincon et al. 2007; Lesur & Ogilvie 2008; Ebrahimi et al. 2009; Bhat et al. 2016;

---

[4] MRI has been studied under varying η before (see Fromang et al. 2007; Fromang & Stone 2009) though not in the context of reconnection.

Ebrahimi & Blackman 2016). In particular, the radially alternating large-scale magnetic fields (as seen in Figures 1(c) and (d)) were also shown through quasilinear theoretical and numerical analyses (Ebrahimi & Blackman 2016).

Before the 3D nonaxisymmetric modes begin to saturate at around $t = 0.7$ ms, we observed some interesting 2D axisymmetric dynamics (see Figure 1(a)). Current sheets start forming near the end of the growth phase of the $n = 0$ mode, around $t = 0.25$ ms. Interestingly, at around $t = 0.35$ ms, there is a slight burst, followed by a quick drop, in the nonaxisymmetric magnetic energy, which resembles a magnetic reconnection event. In order to understand these dynamics, we performed a systematic 2D numerical study, as described in the previous section. The evolution of magnetic energy in the 2D axisymmetric simulations looks similar to that of Figure 1(b), as one might expect.

Below, we first discuss the process of current sheet formation during our axisymmetric simulations. The dynamics and the nonlinear evolution of current sheets are then discussed for simulations at low S when current sheets merge and at high S when current sheets break due to plasmoid instability. Finally, we show that 3D turbulent effects vertically stretch and dissipate formed current sheets, and produce large magnetic islands in the outer regions of the disk and small islands in the inner region of the toroidal plane.

3.1. Current Sheet Formation due to Axisymmetric MRI

In both our 2D and 3D simulations, when the $n = 0$ axisymmetric mode is dominant, we observe the formation of toroidal current sheets. As MRI sets in, a radial perturbation develops in the otherwise vertical magnetic field, as seen in Figure 2(a). According to Ampére's Law, toroidal current density is given as $\mu_0 J_\phi = \partial B_r / \partial z - \partial B_z / \partial r$. In the thin space between the positive and negative regions of B_r (radial magnetic field perturbation fully generated by MRI), the first term on the right grows very large, causing a relatively strong toroidal current J_ϕ to form, as shown in Figure 2(b). These Harris-type current sheets, localized vertically as the result of large gradient in B_r, appear near the end of the growth phase for the $n = 0$ mode. We again emphasize that these current sheets are axisymmetric and form in all our 2D and 3D cases (when $n = 0$ is dominant), however, their dynamics vary based on the Lundquist number and the number of significant toroidal modes, as described below. We should also note that in 2D, current sheets are formed as the result of a steep vertical gradient in large-scale axisymmetric MRI perturbation, and the number of current sheets formed here depends on the vertical wavenumber of the primary MRI mode (and thus the aspect ratio of the system).

3.2. Current Sheet Mergers at Low S

As we investigated the dynamics of current sheets formed around the time of the burst in Figure 1(a), we noted that one of the current sheets moves toward another, colliding with it and combining into one current sheet. See Figure 3(a) for a snapshot of this merging in progress. This is, in part, a product of the attractive Lorentz force felt by two parallel sheets of current moving in the same direction. We observed merging in all of our simulated disks. For the 3D case and 2D cases with $S > 3 \times 10^2$ $(\eta < 5\,\mathrm{m^2\,s^{-1}})$, this merging causes plasmoid formation (closed magnetic loops) due to pinching and compression of magnetic field, as seen in Figure 3(b) (the spot where the magnetic fields are pinched together is often referred


(a)

(b)
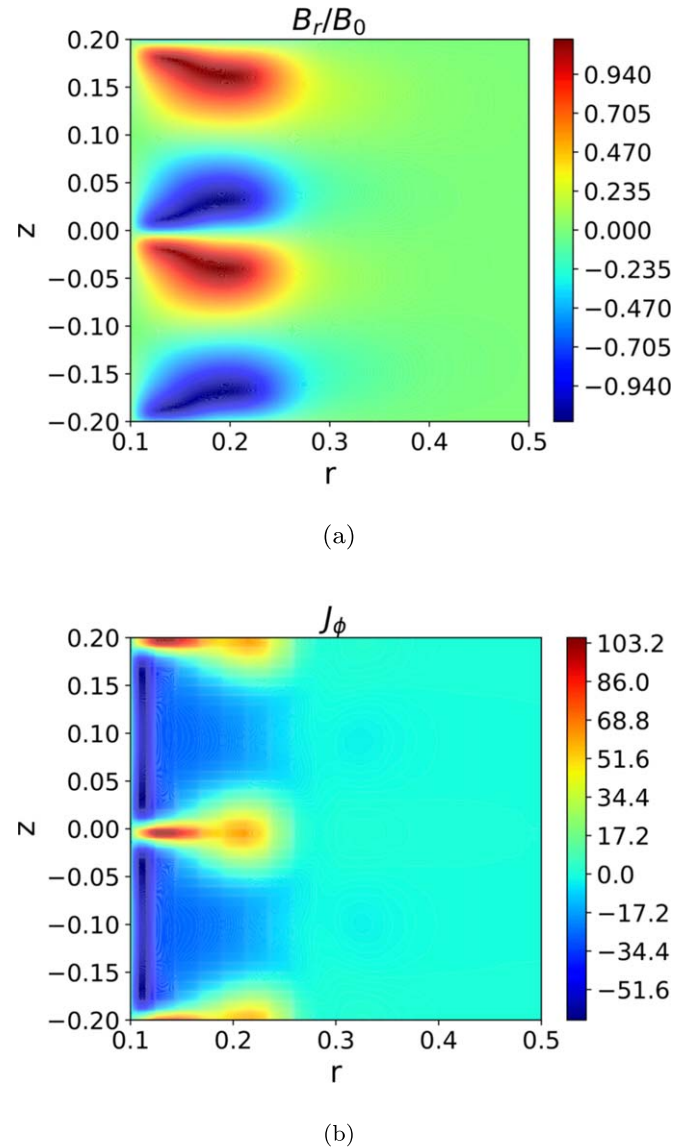
Figure 2. The radial component of the magnetic field, B_r, is shown in (a), normalized by B_0 early in time for disk P1. The corresponding toroidal current density J_ϕ is shown in (b), in units of kilo-amps per meter squared (we will continue to use these units for current density in future plots unless otherwise stated).

to as an X-point). Thus, the merging of current sheets acts as a catalyst for magnetic reconnection.

We can determine what effect the mergers have on angular momentum transport by calculating the $r\phi$ component of the Maxwell stress tensor: $\sigma_{r\phi} = B_r B_\phi / \mu_0$. Negative stress corresponds to outward momentum transport (see Balbus & Hawley 1998). During the merging process, the magnitude of the Maxwell stress increases significantly, by roughly three times its starting magnitude, in the merging region (see Figures 3(c) and (d)). This local burst in momentum transport is consistent with the findings of Ebrahimi & Prager (2011). There, the radially localized current sheets caused outward momentum transport from the tearing modes in a disk.

3.3. Onset of Plasmoid Instability at High S

In addition to merging of current sheets and the formation of closed flux regions (driven plasmoid formation) as shown in
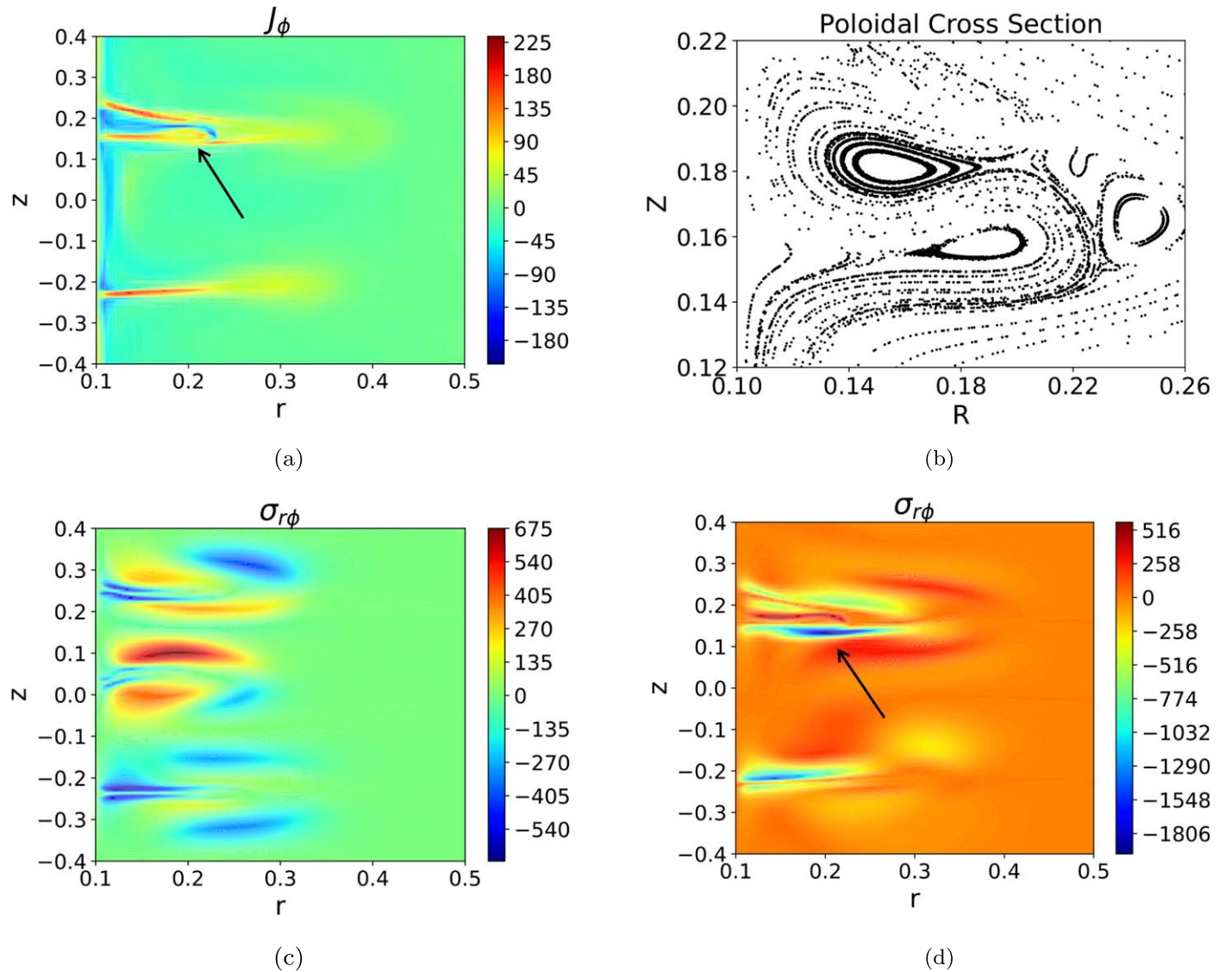
Figure 3. The current density J_ϕ during a merging event for the 3D case at time $t = 0.385$ ms is shown in (a). The black arrow points to the merging region. The corresponding Poincaré plot of the magnetic field is given in (b), zoomed around the region with the two upper current sheets shown by an arrow. The Maxwell stress $\sigma_{r\phi}$ is show in (c) prior to merging, at time $t = 0.320$ ms, while (d) is the Maxwell stress at the time shown in (a) and (b), where the black arrow points to the region of merging.

Figure 3(b), we also observe additional dynamics at high Lundquist number in the 2D regime. Spontaneous plasmoids appear in the current sheets. At Lundquist numbers of 10^3 and up, at least one plasmoid can appear in a current sheet. At 5×10^3 and up, two plasmoids can appear. At 1.4×10^4, we have observed up to four plasmoids form in a sheet. See Figure 4(a) for a plot of the maximum number of plasmoids we observed to form in a current sheet for each 2D simulation. As expected from the theoretical scaling, the number of plasmoids increases with S. Note that the scaling of $S^{3/8}$ is only shown for comparison (Tajima & Shibata 1997). Figures 5(a) and (b) are Poincaré plots of the magnetic field when there are two and four plasmoids present, respectively. Notice that in each case there are multiple X-points, where the magnetic field is getting pinched. There is one plasmoid in particular that is larger than the rest, and this is often referred to as the primary, or "monster," plasmoid (Uzdensky et al. 2010). Multiple plasmoids with multiple X-points is a sign that the current sheets are undergoing

plasmoid instability (Biskamp 1986; Tajima & Shibata 1997; Shibata & Tanuma 2001; Loureiro et al. 2007; Bhattacharjee et al. 2009; Cassak et al. 2009; Samtaney et al. 2009; Huang & Bhattacharjee 2010; Ji & Daughton 2011; Loureiro et al. 2012; Murphy et al. 2013; Yu et al. 2014; Ebrahimi & Raman 2015; Ni et al. 2015; Tenerani et al. 2015; Comisso & Grasso 2016).

We have also estimated the MRI-driven reconnection times for a few of the simulations and included them in Figure 4(b). These rates were computed by finding the difference in time between the formation of the X-point and the appearance of the primary plasmoid. As expected, the reconnection time is roughly proportionate to the Sweet–Parker (Parker 1957; Sweet 1958) scaling of $S^{1/2}$ before the onset of plasmoid instability. We should stress that these times are only a rough estimate; however, they do show that as S becomes larger the reconnection time starts to become weakly dependent on S (Bhattacharjee et al. 2009; Daughton et al. 2009; Huang & Bhattacharjee 2010; Ebrahimi & Raman 2015). As our

(a)

(b)
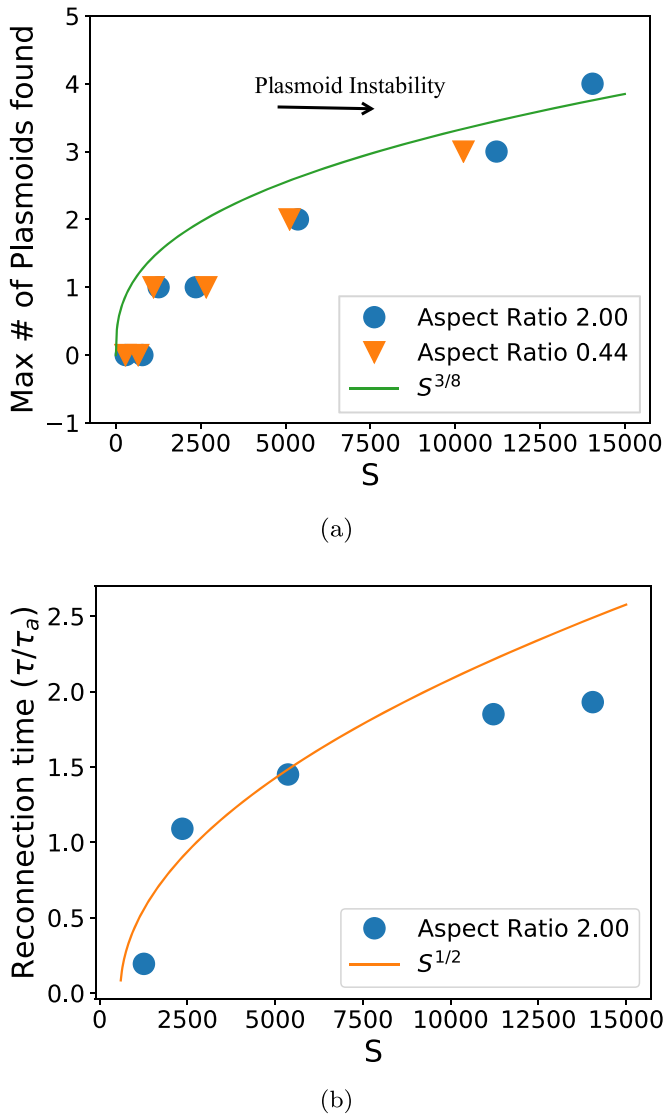
Figure 4. The maximum number of plasmoids in a current sheet from our 2D simulations for a given Lundquist number S with both aspect ratios are shown in (a). The origin of the black arrow denotes the start of plasmoid instability, and it points in the direction of increasing S. The green curve is the theoretical scaling $S^{3/8}$, included for comparison to show the trend of increasing number of plasmoids with local S. Note that it is not a rigorous fit; more data is required. The estimated MRI-driven reconnection times for the taller disk, normalized by the Alfvén time (computed locally as $\tau_A = L/V_A$) are shown in (b). The orange line is a fit of the S-P theoretical scaling $S^{1/2}$, included for comparison.

simulations are global, to further obtain data at higher values of local S shown in Figure 4, much higher poloidal resolution around the 2D MRI-driven current sheets is required.

In addition to an increased number of plasmoids and faster reconnection rates, the current sheets themselves become thinner and more unstable at high Lundquist number. Comparing Figure 2(b) to Figure 5(c), it is clear that the formed current sheets are significantly thinner in the latter plot, at higher Lundquist number. Not long after the current sheets have formed they break into loops as the plasmoids form, as shown in Figure 5(b). Thinner, Sweet–Parker (S-P) type sheets (Parker 1957; Sweet 1958) are observed between plasmoids, as the primary current sheet breaks. Breaking current sheets is another sign of plasmoid instability.

Finally, another signature of spontaneous reconnection is outflows at the X-points, and we identify this along the primary current sheet. When magnetic reconnection occurs, magnetic energy is converted into kinetic energy in the plasma, inducing a flow parallel to the plane of the current sheet. As can be seen in Figure 5(e), this does in fact occur, with the plasma flowing radially inward left of the primary X-point and outward right of the X-point. Interestingly, a short while after the appearance of the plasmoids, as seen in Figure 5(f), the flow changes to be fully outward in the current region. Further detailed analysis of momentum transport and the reconnection rates at yet higher R_m and S remain for a future work.

3.4. Nonaxisymmetric Effects

As the higher nonaxisymmetric n toroidal modes grow and saturate, the plasma flow becomes more turbulent. The remaining current sheets in the poloidal plane at this time have merged and now get stretched vertically (see Figure 6(a)), becoming a 3D current sheet, or filament. These filaments are later dissipated. Interestingly, though we do not show it here, Poincaré plots of the magnetic field in the poloidal plane reveal that a large island forms around this time near the radial edge of the disk.

Plasma current activity also rises in the toroidal plane, as seen in Figure 6(b), with toroidally extending J_z sheets swirling around the center of the disk and diffusing outward. In time this swirl of J_z rotates around the center of the disk. This is consistent with the work of Machida & Matsumoto (2003), who also observed spiraling current density in the in-fall region of the disk. The appearance of this current density J_z is significant, as current in the z direction is important for current outflows in astrophysical jets (Dal Pino 2005; Blackman & Lebedev 2020, and references therein).

The Poincaré plot in the toroidal plane at this time, seen in Figure 6(c) also exhibits magnetic reconnection activities. First, there are small islands near the center of the disk. This is due to the reconnection occurring along the vertical current sheets in the inner region seen in Figure 6(b). Second, a large-scale closed flux surface also appears, which is due to the $n = 1$ nonaxisymmetric mode activity. This structure over time compresses into a smaller, double-island structure as turbulence evolves.

Toward the end of the simulation, as the higher modes become dominant, particularly the $n = 2$ and $n = 3$ modes, toroidal current sheets reappear in the poloidal plane, as seen in Figure 6(d) at $t = 1.22$ ms. These sheets are far more dynamic at this time, however, due to the turbulent flows. They flap up and down, and every so often they eject current in a cloud (currently happening in the bottom left sheet in Figure 6(d)). At this time, additional turbulent spirals of J_z also appear near the center in the toroidal plane as well, as seen in Figure 6(e). More large islands spawn in the toroidal plane, as seen in Figure 6(f). These 3D island structures are likely generated due to a combination of current sheet reconnection and turbulent driven magnetic reconnection (Lazarian & Vishniac 1999) from $n = 2$ and $n = 3$ fluctuations.

4. Summary and Conclusions

In the framework of a resistive MHD model, we have numerically studied the evolution of current and magnetic field in 2D accretion disks and a 3D disk subject to a vertical seed
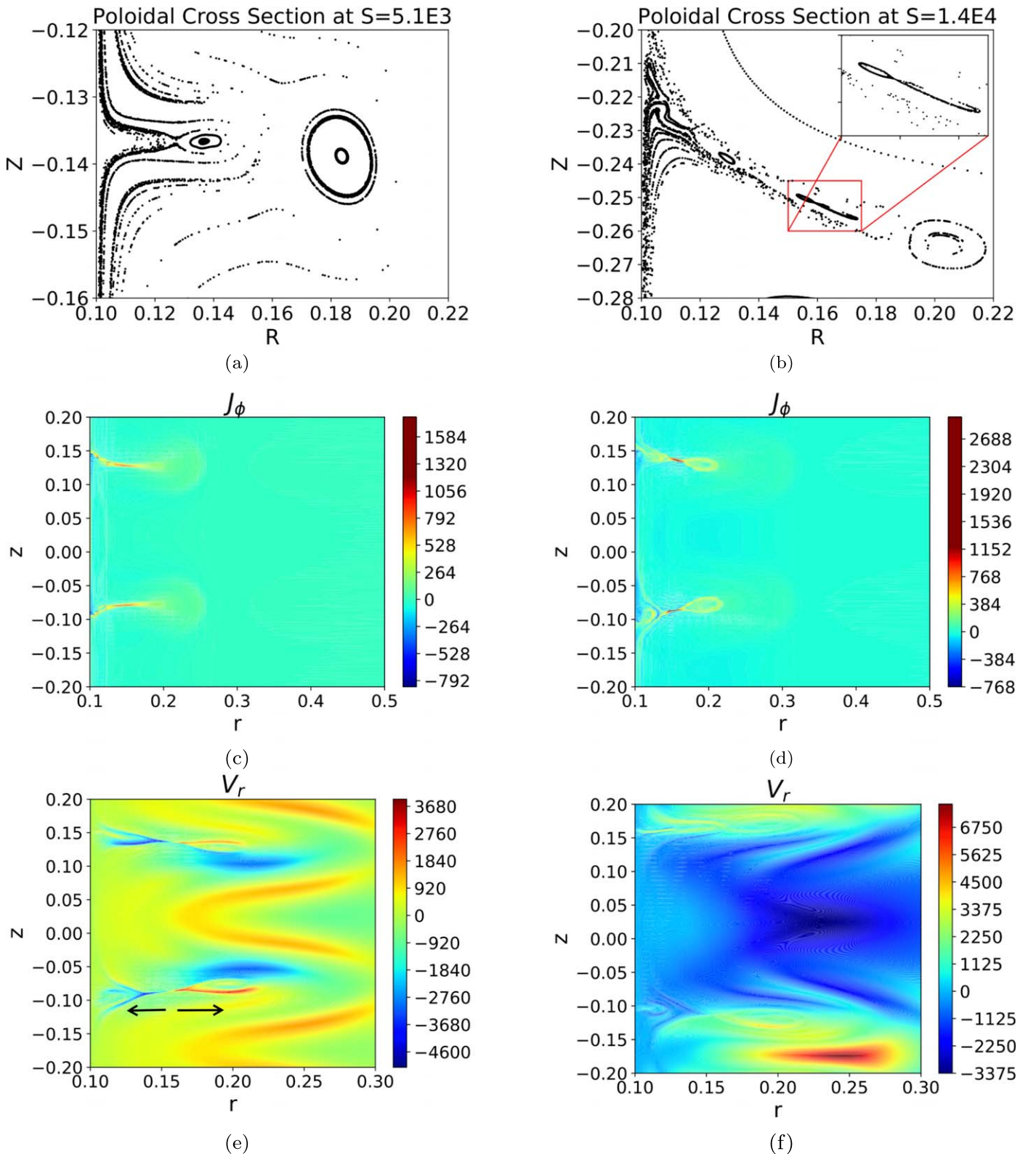
Figure 5. (a) Poincaré plot of the magnetic field around a current sheet containing two plasmoids in disk P5. (b) Magnetic field around a current sheet containing four plasmoids in disk O7. (c) Toroidal current density just after the current sheets have formed for disk P6. (d) Toroidal current density in disk P6 just after plasmoids form. (e) The radial plasma flow V_r at the time shown in (d). The arrows denote the direction of flow around the X-point in the lower current sheet. (f) The radial plasma flows a few timesteps after the plasmoids appeared.

magnetic field. In doing so we have made four key observations. First, we found that MRI induces radial perturbations in the magnetic field, creating toroidal Harris-type current sheets. This proves that MRI is a driver for current sheets in astrophysical

disks (as we call MRI-driven current sheets). Second, these current sheets are drawn to one another by a Lorentz force and merge, driving magnetic reconnection and local momentum transport at $S > 3 \times 10^2$. This process is a source of plasmoids that
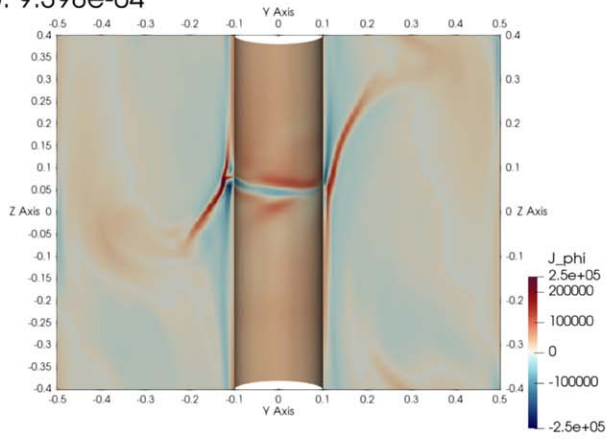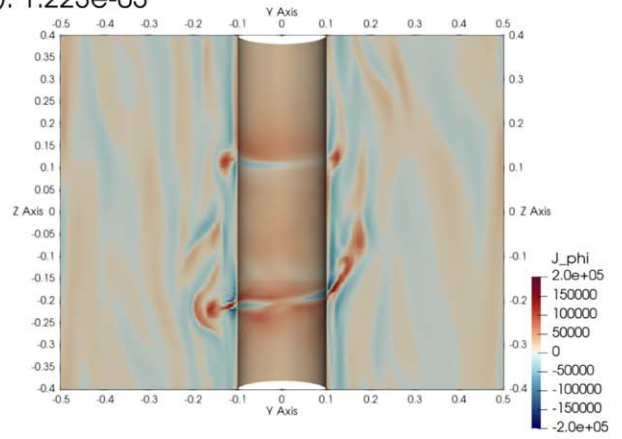
(a)

(d)

(b)

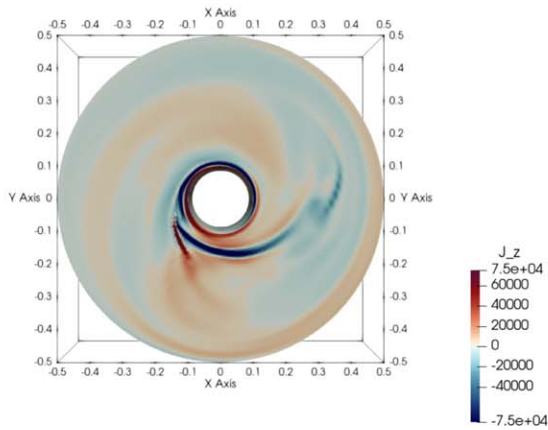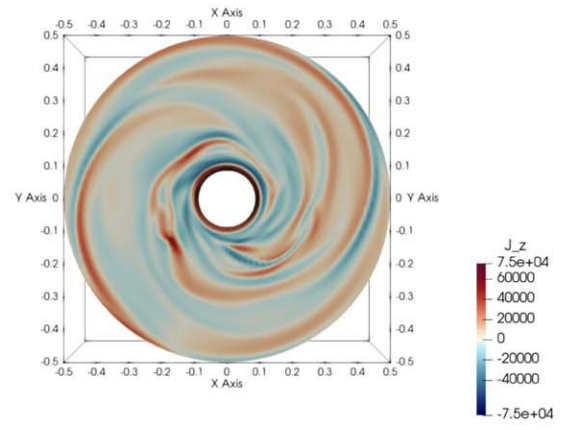

(e)

(c)
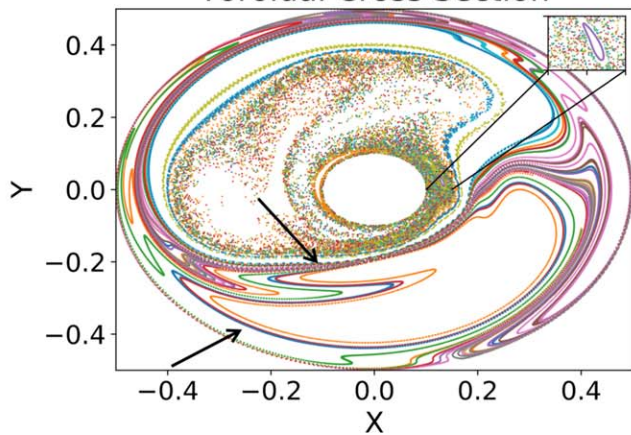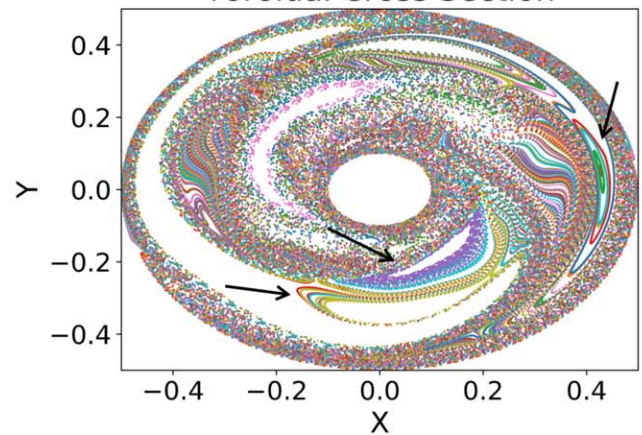
(f)

Figure 6. Current densities and Poincare plots for the 3D case during saturation at two times: (a)–(c) are taken at $t = 0.9398$ ms, and (d)–(f) are taken at $t = 1.223$ ms. (a) and (d) are the vertically extended current densities J_ϕ in a poloidal cut. (b) and (e) are the vertical current densities J_z in a toroidal cut. (c) and (f) are the Poincaré plots in the toroidal plane. The black arrows point to the large magnetic island structure.

could be contributing to flares and gamma-ray emissions (Singh et al. 2015; Ripperda et al. 2020) and extreme particle acceleration (Uzdensky et al. 2011; Cerutti et al. 2014; Sironi et al. 2016).

Third, at $S \geqslant 5 \times 10^3$, the current sheets become thin and subject to plasmoid instability driven by MRI, breaking into multiple plasmoids. This is significant, as it shows that MRI itself can lead to plasmoid instability, even in the absence of other effects such as general relativity or nonideal MHD. This is the first demonstration of formation of current sheets driven by large-scale primary (axisymmetric) MRI mode (see Figure 2(a)), and the subsequent breaking of these current sheets due to spontaneous plasmoid reconnection (tearing instability—Furth et al. 1963—in a current sheet). Our calculation of reconnection times also approximately follows the theoretical scaling of $S^{1/2}$ at low S, but starts to show weak dependency on S with the onset of plasmoid instability. The impact of the plasmoid instability on the MRI saturation mechanism and its effect on momentum transport will remain for a future study.

Finally, once nonaxisymmetric effects become significant, turbulence stretches the remaining current sheets vertically and dissipates them, and large magnetic islands form in the outer regions of the disk in both the poloidal and toroidal plane. In addition, smaller plasmoids form near the center of the disk in the toroidal plane due to reconnection along vertical current sheets. These vertical currents (generated by the large-scale azimuthal dynamo fields) are important for current outflows in astrophysical jets and the disk corona region (Dal Pino 2005; McKinney & Blandford 2009; Blackman & Lebedev 2020). Eventually, toroidal current sheets reappear in the poloidal plane but are unstable to the plasma flow.

In summary, based on a first-principle approach using resistive MHD solutions, it is found that initial field lines threading a differentially rotating disk are stretched radially and toroidally outward by the primary MRI mode[5] to produce radially extended azimuthal current sheets (and reconnection sites with oppositely directed field lines), which break into plasmoids at high local Lundquist number. With our cylindrical disk model, we have uncovered some of the fundamental reconnection processes triggered or driven by MRI. By examining the current evolution in the poloidal and toroidal planes and following the magnetic field lines in both 2D and 3D simulations, we have identified sites of fast plasmoid reconnection (Bhattacharjee et al. 2009; Huang & Bhattacharjee 2010; Loureiro et al. 2012; Ebrahimi & Raman 2015), as well as 3D reconnection sites potentially due to turbulent reconnection and nonaxisymmetric fluctuations. In this paper, we have not focused on small-scale MRI turbulence and the associated power spectrum. Although turbulent reconnection (Lazarian & Vishniac 1999; Kowal et al. 2009; Eyink et al. 2011; Kadowaki et al. 2018; Jafari et al. 2020; Lazarian et al. 2020) is relevant, it is not the primary driver of reconnection in our 2D simulations. In our 3D simulations, however, small-scale turbulence could play a role. For example, small-scale 3D disturbances around the Harris-type current sheets could enhance local S to trigger fast reconnection (Ebrahimi 2016). Here on the other hand, it is hard to differentiate between the driven turbulence reconnection versus the spontaneous plasmoid reconnection due to MRI. We believe both occur in our 3D simulations, but further simulations are required to identify the role of small-scale turbulence on the reconnection rate.

Lastly, we should note that our cylindrical disk model may have some limitations, but on the other hand provides solutions in a real global domain with curvature terms and explicit resistivity and viscosity. Our focus here has been to capture the associated reconnection physics of MRI in cylindrical differentially rotating plasmas. Further detailed 3D simulations including other physics such as nonideal effects, stratification, and higher magnetic Reynolds number will be investigated in future work.

ORCID iDs

Jarrett Rosenberg ⓘ https://orcid.org/0000-0001-7468-7261
Fatima Ebrahimi ⓘ https://orcid.org/0000-0003-3109-5367

References

Balbus, S. A., & Hawley, J. F. 1991, ApJ, 376, 214
Balbus, S. A., & Hawley, J. F. 1998, RvMp, 70, 1
Bhat, P., Ebrahimi, F., & Blackman, E. G. 2016, MNRAS, 462, 818
Bhattacharjee, A., Huang, Y.-M., Yang, H., & Rogers, B. 2009, PhPl, 16, 112102
Biskamp, D. 1986, PhFlB, 29, 1520
Blackman, E. G., & Lebedev, S. V. 2020, arXiv:2009.08057
Brandenburg, A., Nordlund, A., Stein, R. F., & Torkelsson, U. 1995, ApJ, 446, 741
Cassak, P. A., Shay, M. A., & Drake, J. F. 2009, PhPl, 16, 120702
Cerutti, B., Werner, G. R., Uzdensky, D. A., & Begelman, M. C. 2014, PhPl, 21, 056501
Comisso, L., & Grasso, D. 2016, PhPl, 23, 032111
Dal Pino, E. M. d. G. 2005, AdSpR, 35, 908
Daughton, W., Roytershteyn, V., Albright, B. J., et al. 2009, PhRvL, 103, 065004
Ebrahimi, F. 2016, PhPl, 23, 120705
Ebrahimi, F. 2020, JPlPh, 86, 905860614
Ebrahimi, F., & Blackman, E. G. 2016, MNRAS, 459, 1422
Ebrahimi, F., Lefebvre, B., Forest, C. B., & Bhattacharjee, A. 2011, PhPl, 18, 062904
Ebrahimi, F., & Prager, S. C. 2011, ApJ, 743, 192
Ebrahimi, F., Prager, S. C., & Schnack, D. D. 2009, ApJ, 698, 233
Ebrahimi, F., & Raman, R. 2015, PhRvL, 114, 205003
Event Horizon Telescope Collaboration, Akiyama, K., Algaba, J. C., et al. 2021, ApJL, 910, L13
Eyink, G. L., Lazarian, A., & Vishniac, E. T. 2011, ApJ, 743, 51
Fox, N. J., Velli, M. C., Bale, S. D., et al. 2016, SSRv, 204, 7
Fromang, S., Papaloizou, J., Lesur, G., & Heinemann, T. 2007, A&A, 476, 1123
Fromang, S., & Stone, J. M. 2009, A&A, 507, 19
Furth, H. P., Killeen, J., & Rosenbluth, M. N. 1963, PhFlB, 6, 459
Goodman, J., & Xu, G. 1994, ApJ, 432, 213
Hawley, J. F., & Balbus, S. A. 1992, ApJ, 400, 595
Huang, Y.-M., & Bhattacharjee, A. 2010, PhPl, 17, 062104
Hubbard, A., McNally, C. P., & Mac Low, M.-M. 2012, ApJ, 761, 58
Jafari, A., Vishniac, E., & Vaikundaraman, V. 2020, PhPl, 27, 072301
Ji, H., Alt, A., Antiochos, S., et al. 2020, arXiv:2004.00079
Ji, H., & Daughton, W. 2011, PhPl, 18, 111207
Kadowaki, L. H. S., De Gouveia Dal Pino, E. M., & Stone, J. M. 2018, ApJ, 864, 52
Kowal, G., Lazarian, A., Vishniac, E. T., & Otmianowska-Mazur, K. 2009, ApJ, 700, 63
Latter, H. N., Lesaffre, P., & Balbus, S. A. 2009, MNRAS, 394, 715
Lazarian, A., Eyink, G. L., Jafari, A., et al. 2020, PhPl, 27, 012305

---

[5] For visualizations of the field lines see Figure 5 in Ref Ebrahimi & Blackman (2016).

Lazarian, A., & Vishniac, E. T. 1999, ApJ, 517, 700
Lesur, G., & Ogilvie, G. I. 2008, A&A, 488, 451
Liu, W., Goodman, J., & Ji, H. 2006, ApJ, 643, 306
Loureiro, N. F., Samtaney, R., Schekochihin, A. A., & Uzdensky, D. A. 2012, PhPl, 19, 042303
Loureiro, N. F., Schekochihin, A. A., & Cowley, S. C. 2007, PhPl, 14, 100703
Machida, M., & Matsumoto, R. 2003, ApJ, 585, 429
McKinney, J. C., & Blandford, R. D. 2009, MNRAS, 394, L126
Murphy, N. A., Young, A. K., Shen, C., Lin, J., & Ni, L. 2013, PhPl, 20, 061211
Ni, L., Kliem, B., Lin, J., & Wu, N. 2015, ApJ, 799, 79
Parker, E. N. 1957, JGR, 62, 509
Petschek, H. E. 1964, NASSP, 50, 425
Rincon, F., Ogilvie, G. I., & Proctor, M. R. E. 2007, PhRvL, 98, 254502
Ripperda, B., Bacchini, F., & Philippov, A. A. 2020, ApJ, 900, 100
Samtaney, R., Loureiro, N. F., Uzdensky, D. A., Schekochihin, A. A., & Cowley, S. C. 2009, PhRvL, 103, 105004
Shibata, K., & Tanuma, S. 2001, EP&S, 53, 473
Singh, C. B., de Gouveia Dal Pino, E. M., & Kadowaki, L. H. S. 2015, ApJ, 799, L20
Sironi, L., Giannios, D., & Petropoulou, M. 2016, MNRAS, 462, 48
Sovinec, C., Glasser, A., Gianakon, T., et al. 2004, JCoPh, 195, 355
Sweet, P. A. 1958, in IAU Symp. 6, Electromagnetic Phenomena in Cosmical Physics, ed. B. Lehnert (Cambridge: Cambridge Univ. Press), 123
Tajima, T., & Shibata, K. 1997, Plasma Astrophysics (Reading, MA: Addison-Wesley)
Tatsuno, T., & Dorland, W. 2008, AN, 329, 688
Tenerani, A., Rappazzo, A. F., Velli, M., & Pucci, F. 2015, ApJ, 801, 145
Uzdensky, D., Loureiro, N., & Schekochihin, A. 2010, PhRvL, 105, 235002
Uzdensky, D. A. 2011, SSRv, 160, 45
Uzdensky, D. A., Cerutti, B., & Begelman, M. C. 2011, ApJL, 737, L40
Yu, Q., Günter, S., & Lackner, K. 2014, NucFu, 54, 072005
Zweibel, E. G., & Yamada, M. 2009, ARA&A, 47, 291